Breaking the quantum adiabatic speed-limit by jumping along geodesics

Kebiao Xu[1,2,4],[*] Tianyu Xie[1,2,4],[*] Fazhan Shi[1,2,4], Zhen-Yu Wang[3],[†] Xiangkun Xu[1,2,4],[‡] Pengfei Wang[1,4], Ya Wang[1,4], Martin B. Plenio[3], and Jiangfeng Du[1,2,4][§]

1. *CAS Key Laboratory of Microscale Magnetic Resonance and Department of Modern Physics,*
University of Science and Technology of China (USTC), Hefei 230026, China
2. *Hefei National Laboratory for Physical Sciences at the Microscale, USTC, Hefei 230026, China*
3. *Institut für Theoretische Physik and IQST, Albert-Einstein-Allee 11, Universität Ulm, D-89069 Ulm, Germany and*
4. *Synergetic Innovation Center of Quantum Information and Quantum Physics, USTC, Hefei 230026, China*

Because of the intrinsic robustness, adiabatic evolutions find a broad range of applications in quantum state engineering [1, 2], quantum computing [3–5], and quantum simulation [6, 7]. According to the original form of the quantum adiabatic theorem, for a process to remain adiabatic, its rate of change at all times must be much smaller than the energy gap of the Hamiltonian [8]. On the other hand, in order to avoid perturbations from the environment high rates of change are desirable. This tension imposes severe limitations on the practical use of adiabatic methods. Current approaches to obtain adiabatic evolution within system coherence times are shortcuts to adiabaticity by using intricate schemes of additional counterdiabatic driving fields [9–15] which however can be exceedingly challenging to implement experimentally. Here, we investigate the roles of energy gaps in quantum adiabatic processes by using a nitrogen-vacancy (NV) centre in diamond [16]. We demonstrate experimentally that energy gaps may vanish while maintaining adiabatic evolution, a result that challenges traditional views. This shows that dynamic phases are more fundamental than energy gaps in quantum adiabatic evolution, the key insight that allows us to overcome the limits on evolution times imposed by the traditional form of the adiabatic theorem and to achieve, within experimental uncertainties, unit fidelity quantum adiabatic processes in finite time. The results provide a deeper understanding on quantum adiabatic processes, as well as promising strategies and directions in the control of quantum systems.

Coherent control on quantum systems is a fundamental element of quantum technologies which could revolutionize the fields of information processing, simulation, and sensing. A powerful and universal method to achieve this control is the quantum adiabatic technique, which exhibits intrinsic robustness against control errors ensured by the quantum adiabatic theorem [17]. The theorem states in its original form that "a physical system remains in its instantaneous eigenstate if a given perturbation is acting on it slowly enough and if there is a gap between the eigenvalue and the rest of the Hamiltonian's spectrum" [8]. The adiabatic evolution itself also provides interesting properties such as Abelian [18] or non-Abelian geometric phases [19], which can be used for the realisation of quantum gates. However, despite the long history and wide range of applications, it was discovered recently that key aspects of quantum adiabatic evolution remain not fully understood [20, 21].

In this work, we experimentally demonstrate adiabatic evolutions with vanishing energy gaps and crossings, by using an NV center in diamond. Additionally, we reveal that employing discrete jumps along the evolution path allows quantum adiabatic processes at unlimited rates which challenges the view that adiabatic processes must be slow. By jumping along the path one can even avoid path points where the eigenstates of the Hamiltonian are not feasible in experiments. Furthermore, we demonstrate theoretically and experimentally the elimination of all the non-adiabatic effects on system evolution of a finite evolution time by driving the system along the geodesic that connect initial and final states, as well as combating system decoherence by incorporating pulse sequences into adiabatic driving.

To describe the theory, consider a quantum system driven by a time-dependent Hamiltonian for adiabatic evolution, with its instantaneous orthonormal eigenstates $|\psi_n(\lambda)\rangle$ $(n = 1, 2, \ldots, M)$ varied along a path parameterized by $\lambda \in [0, 1]$. For arbitrary driving, all the non-adiabatic effects are completely described by the gauge-invariant propagator $U_{\text{dia}}(\lambda)$, which satisfies the first-order differential equation [22]

$$\frac{d}{d\lambda}U_{\text{dia}}(\lambda) = iW(\lambda)U_{\text{dia}}(\lambda), \qquad (1)$$

with the boundary condition that $U_{\text{dia}}(\lambda = 0) = I$ is an identity matrix (i.e., no non-adiabatic effect). In the basis of $|\psi_n(0)\rangle$, the diagonal matrix elements of $W(\lambda)$ vanishes, i.e., $\langle\psi_n(0)|W(\lambda)|\psi_n(0)\rangle = 0$. The off-diagonal matrix elements

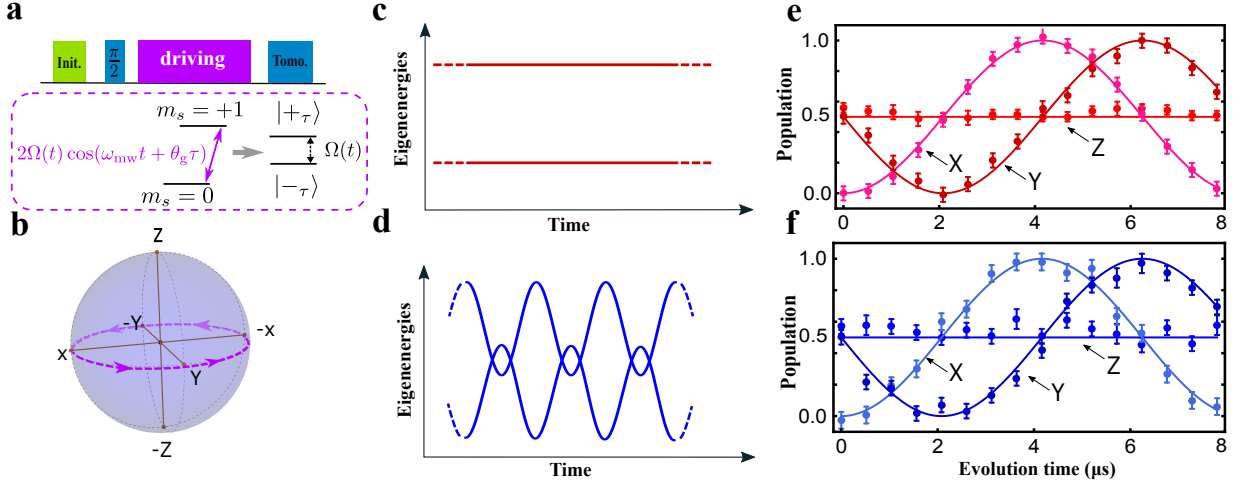$$\langle\psi_n(0)|W(\lambda)|\psi_m(0)\rangle = F_{n,m}(\lambda)G_{n,m}(\lambda) \qquad (2)$$

FIG. 1. **Adiabatic evolution by continuous driving. a**, Illustration of the experimental control. A microwave on-resonant to a NV transition forms two microwave dressed states $|\pm_\lambda\rangle$ with a tunable energy gap corresponding to the Rabi frequency Ω. Changing the parameter λ from 0 to 1 in the microwave phase realizes the path depicted on the Bloch sphere in **b**, which starts from and comes back to the point X after a circle with $\theta_g = 2\pi$ and a changing rate $d\lambda/dt = 0.12$ MHz. **c**, The energies of the dressed states $|\pm_\lambda\rangle$ for a constant Rabi frequency $\Omega(t) = \Omega_0$. **d**, Same as **c** but the gap is varied as $\Omega(t) = \Omega_\pi(t)$ by using a time-dependent Rabi frequency. **e** and **f** show the state tomography for the cases of **c** and **d**, respectively. The lines are the ideal adiabatic cases and the dots are experimental data. The error bars in all the figures represent two standard deviation of uncertainty.

are responsible for non-adiabaticity. Here the factor

$$F_{n,m}(\lambda) = e^{i[\phi_n(\lambda) - \phi_m(\lambda)]} \qquad (3)$$

is described by the accumulated dynamic phases $\phi_n(\lambda)$ on $|\psi_n(\lambda)\rangle$, and $G_{n,m}(\lambda) = e^{i[\gamma_n(\lambda) - \gamma_m(\lambda)]} g_{n,m}(\lambda)$ is the geometric part consisting of the geometric functions $g_{n,m}(\lambda) = i\langle\psi_n(\lambda)|\frac{d}{d\lambda}|\psi_m(\lambda)\rangle$ and the geometric phases $\gamma_n(\lambda) = \int_0^\lambda g_{n,n}(\lambda')d\lambda'$.

Equations (2) and (3) show that the differences of dynamic phases are more fundamental than the energy gaps in suppressing the non-adiabatic effects. Indeed, a recent theoretical paper [22] provided for the first time a necessary and sufficient condition for quantum adiabatic evolution along the whole path. It states that when

$$\left| \int_0^\lambda F_{n,m}(\lambda')d\lambda' \right| < \epsilon, \qquad (4)$$

for any $\lambda \in [0,1]$ of a finite path the deviation from adiabaticity is proportional to ϵ and can hence be made arbitrarily small for $\epsilon \to 0$ to achieve $U_{\mathrm{dia}}(\lambda) \to I$ along the entire path [22].

In the traditional approach that the Hamiltonian varies slowly with non-vanishing gaps (e.g., Fig. 1c), the strength of relative dynamic phase $|\phi_n(\lambda) - \phi_m(\lambda)|$ rapidly increases with the change of the path parameter λ, giving the fast oscillating factors $F_{n,m}(\lambda)$ and thus suppressing non-adiabatic transitions.

In contrast, here we demonstrate experimentally that adiabatic evolution can be achieved even for vanishing energy gaps and crossings for as long as equation (4) is

satisfied. As an example, we consider the energy gap of the form $\Omega(t) = \Omega_\pi(t) \equiv \Omega_0 [1 + a \cos(2\Omega_0 t)]$, which has zeros and crossings for $|a| > 1$ (see Fig. 1d for the case of $a \approx 2.34$). However, the corresponding factors $F_{n,m}(\lambda)$ parameterized by the parameter $\lambda = t/T$ can satisfy the condition (4). In order to realise this energy gap experimentally, we apply a microwave field that is resonant to the transition of the NV electron spin states $|m_s = 0\rangle \equiv |-z\rangle$ and $|m_s = +1\rangle \equiv |z\rangle$ to forms the parameterized dressed states

$$|\pm_\lambda\rangle = \frac{1}{\sqrt{2}}(|z\rangle \pm e^{i\theta_g\lambda}|-z\rangle). \qquad (5)$$

In the dressed-state picture the Rabi frequency $\Omega(t)$ of the driving field becomes the energy gap of the dressed states (see Fig. 1a). With a sufficiently large T, the system evolutions for a constant gap $\Omega(t) = \Omega_0$ (corresponding to a constant Rabi frequency, see Fig. 1c,e) and for the time-dependent gap $\Omega(t) = \Omega_\pi(t)$ (corresponding to a time-dependent Rabi frequency, see Fig. 1d,f) follow the adiabatic states at all times with high fidelities.

Without the restriction to non-zero energy gaps, it is possible to completely eliminate non-adiabatic effects and to drive an arbitrary initial state $|\Psi_i\rangle$ to a target state $|\Psi_t\rangle$ by the adiabatic evolution of a finite time duration. We demonstrate this by driving the system along the geodesic [23, 24] for maximal speed. As shown in Methods, the system eigenstate $|\psi_1(\lambda)\rangle = \cos(\frac{1}{2}\theta_g\lambda)|\psi_1(0)\rangle + \sin(\frac{1}{2}\theta_g\lambda)|\psi_2(0)\rangle$ connects $|\psi_1(0)\rangle$ and $|\psi_1(1)\rangle$ along the geodesic by varying $\lambda = 0$ to $\lambda = 1$, with its orthonormal eigenstate $|\psi_2(\lambda)\rangle = -\sin(\frac{1}{2}\theta_g\lambda)|\psi_1(0)\rangle + \cos(\frac{1}{2}\theta_g\lambda)|\psi_2(0)\rangle$ varied accordingly.
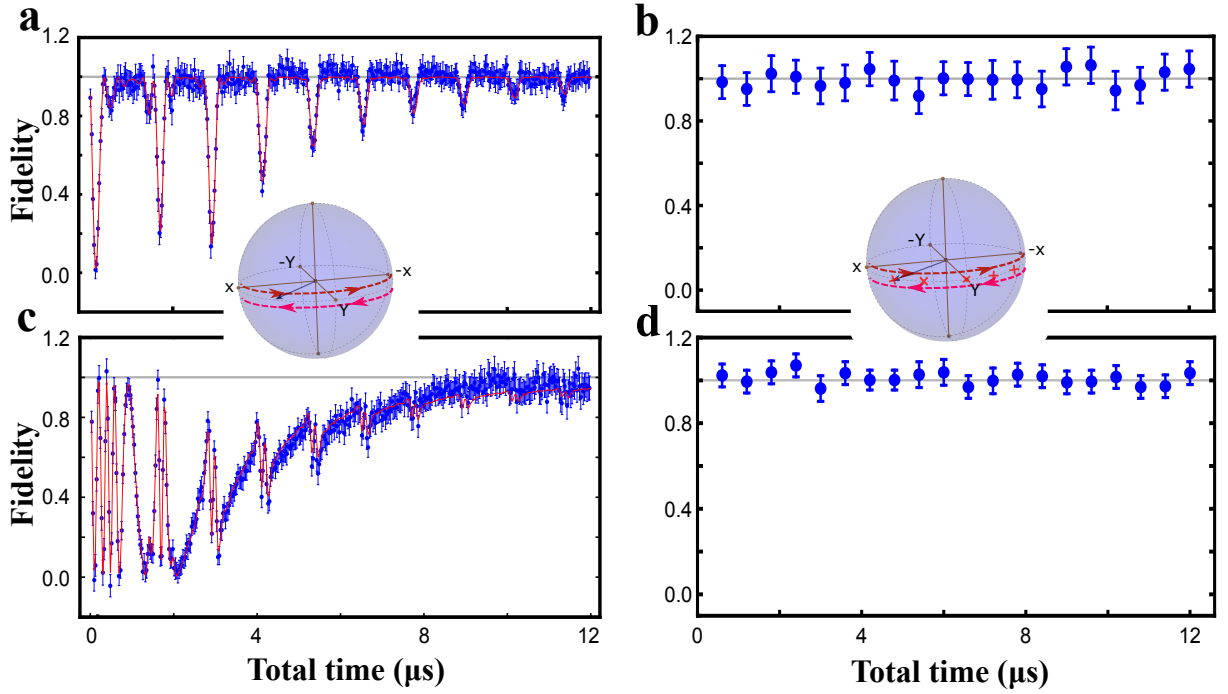
FIG. 2. **High-fidelity adiabatic protocol along geodesics. a,c** and **b,d** show the final state fidelity to the target adiabatic state as a function of the total time by using the continuous and jumping protocols, respectively. The target state is defined as the state driven by ideal, infinitely slow adiabatic evolution. The insets illustrate the path that proceeds from the X direction (corresponding to the state $|+_0\rangle = |x\rangle$ on the Bloch sphere) to the $-$X direction (corresponding to $|-_0\rangle = |-x\rangle$) via a geodesic half circle then travels back to X and repeats the back-forward motion for three times. The continuous protocol (**a,c**) has a constant gap ($\Omega_0 = 2\pi \times 5$ MHz) , while in the jumping protocol (**b,d**) the π pulses have the same amplitude as the continuous protocol but are applied at the path points λ_j without time delay. The path points for $N = 5$ are indicated by the crosses on the Bloch sphere in the inset on top of **b** and **d**. In **a** and **b** the initial state is prepared in an initial eigenstate $|x\rangle$, while **c** and **d** are the results when the initial state starts from $|y\rangle = \frac{1}{\sqrt{2}}(|x\rangle + |-x\rangle)$, which is an equal superposition of the initial eigenstates. The red lines in **a** and **c** show the fidelities between the numerical simulated state and the target state. The numerical simulation has taken experimental noise sources into consideration, and details about the noise model can be found in Methods (numerical simulations). The horizontal grey lines in all the figures indicate the level of unit fidelity.

An example of the geodesic path is given by equation (5). We find that along the geodesic the only nonzero elements $g_{2,1}(\lambda)$ and $g_{1,2}(\lambda)$ are constant. We adopt the sequence theoretically proposed in Ref. 22 that changes the dynamic phases at N equally spaced path points $\lambda = \lambda_j$ ($j = 1, 2, \ldots, N$). By staying at each of the points

$$\lambda_j = (2N)^{-1}(2j - 1), \qquad (6)$$

for a time required to implement a π phase shift on the dynamic phases, we have $U_{\text{dia}}(1) = I$ because $W(\lambda)$ commutes and $\int_0^1 F_{2,1}(\lambda)d\lambda = 0$. That is, by jumping on discrete points λ_j the system evolution at $\lambda = 1$ is exactly the perfect adiabatic evolution U_{adia} even through the evolution time is finite, and an initial state $|\Psi_i\rangle$ will end up with the adiabatic target state $|\Psi_t\rangle = U_{\text{adia}}|\Psi_i\rangle$. To realize the jumping protocol in experiments, we apply rectangular π pulses at the points λ_j without time delay between the pulses.

We measure the fidelity of the evolved state to the target state $|\Psi_t\rangle$ that follows the ideal adiabatic evolution U_{adia} and compare the performance between the jump-

ing protocol and the continuous one that has a constant gap and a constant sweeping rate. The evolution path is the geodesic given by equation (5). To show the performance in the high-fidelity regime, in Fig. 2 we traverse the half-circle path with $\theta_g = \pi$ back and forth for a total path length of $6\theta_g$, while the results for the path of a single half circle is presented in Supplementary Fig. 8. The jumping protocol reaches unit fidelity within the measurement accuracy, while the standard continuous driving has lower fidelity at short evolution times. We observe in Fig. 2a that the constant-gap protocol provides unit state-transfer fidelity only when the initial state is an eigenstate of the initial Hamiltonian $|\Psi_i\rangle = |+_0\rangle$ and the relative dynamic phase $\phi = \sqrt{(2k\pi)^2 - (\theta_g)^2}$ ($k = 1, 2, \ldots$) accumulated in a half circle (see Methods). However, the phase shifts on the system eigenstates accompanying adiabatic evolution can not be observed when the initial state is prepared in one of the initial eigenstates. Therefore, we also compare the fidelities in Fig. 2c,d by using an initial state $|\Psi_i\rangle = |+_{1/2}\rangle$, which is a superposition of the initial eigenstates $|\pm_0\rangle$. The

results of Fig. 2b,d confirm that the jumping protocol achieves exactly the adiabatic evolution U_{adia} within the experimental uncertainties. To further check the adiabaticity during the whole evolution process, we carried out the measurement for a fixed $N = 5$, the results in Supplementary Fig. 7 do reveal the adiabaticity and the advantage of the jumping protocol over the standard one.

To demonstrate the intrinsic robustness guaranteed by adiabatic evolutions, in Fig. 3, we consider large random driving amplitude errors in the jumping protocol. We add random Gaussian distributed errors with a standard deviation of 50 % to the control amplitude. To simulate white noise, we change the amplitude after every 10 ns in an uncorrelated manner. Despite the large amplitude errors, which can even cause energy crossings, that is vanishing energy gaps, during the evolution (see Fig. 3a for a random time trace), a change of fidelity is hardly observable in Fig. 3b. Additional simulations in Supplementary Figs. 10 and 11 also demonstrate the robustness for amplitude fluctuations of different kinds of noise correlation, i.e., Gaussian white noise, Ornstein-Uhlenbeck process modelled noise, and static random noise. Because the pulses suppress the effect of decoherence with the mechanism of dynamical decoupling [25], the fidelity is still high even when the evolution time is much longer than the coherence time $T_2^* = 1.7$ μs of the NV electron spin (Supplementary Fig. 9). This evidence is useful to design adiabatic protocols that provide strong robustness against both control errors and general environmental perturbations.

Without going through all the path points, the jumping protocol has advantages to avoid path points (i.e., Hamiltonian with certain eigenstates) that can not be realized in experiments. As a proof-of-principle experiment, we consider the Landau-Zener (LZ) Hamiltonian [26] $H_{\text{LZ}} = B_z(\lambda)\frac{\sigma_z}{2} + \Delta\frac{\sigma_x}{2}$ with σ_α ($\alpha = $ x, y, z) being the Pauli matrices. Because $\Delta > 0$, tuning the system eigenstates to the eigenstates $|\pm z\rangle$ of σ_z requires $B_z \to \pm\infty$. Therefore for a perfect state transfer from $|\Psi_i\rangle = |-z\rangle$ to $|\Psi_t\rangle = |z\rangle$ by using the standard continuous protocol, it is required to adiabatically tune B_z from $-\infty$ to $+\infty$ (see insets of Fig. 4a). The experimental implementation of $B_z = \pm\infty$ however requires an infinitely large control field, which is a severe limitation. In our experiment, a large B_z field can be simulated by going to the rotating frame of the microwave control field with a large frequency detuning. The experimental realization of $B_z \to \pm\infty$ can be challenging in other quantum platforms. For example, for superconducting qubits where $\Delta/(2\pi)$ could be as large as 0.1 GHz but the tuning range of $B_z/(2\pi)$ is usually limited to a couple of GHz or even of the same order of magnitude as $\Delta/(2\pi)$ [27]. For two-level quantum system comprising Bose-Einstein condensates in optical lattices, the maximum ratio of B_z/Δ is determined by the band structure [12]. For singlet-triplet qubits in semiconductor quantum dots, the exchange interaction for the control of B_z is positively confined [28]. On the contrary, with the jumping approach, one can
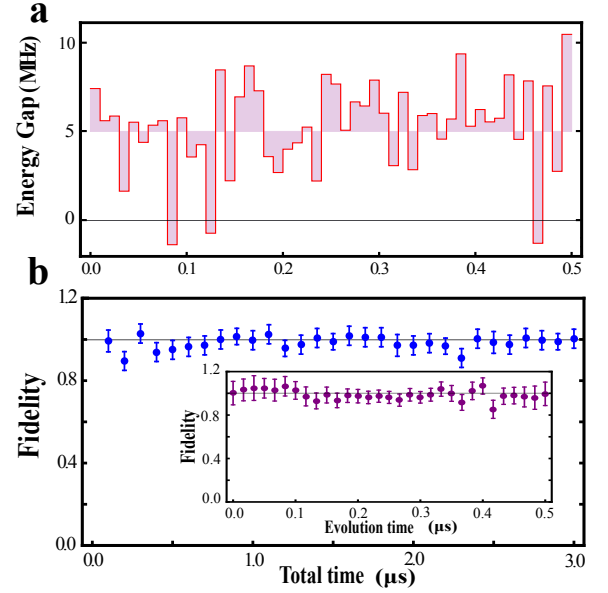

FIG. 3. **Robustness of the jumping protocol. a,** Exemplary time trace of the driving Rabi frequency. The amplitudes of the Rabi frequency (i.e., energy gap) is randomly generated by the Gaussian distribution with a mean of $2\pi \times 5$ MHz and a standard deviation of $2\pi \times 2.5$ MHz. The amplitudes are uncorrelated at every slices of duration of 10 ns. **b,** Final state fidelity as a function of the total time using the amplitudes as **a** and the initial state prepared in the eigenstate $|+_0\rangle$. **Inset of b** shows the fidelity during the evolution time for $N = 5$. The fidelities are measured by the experimental state to the ideal state under infinitely slow adiabatic evolution.

avoid the unphysical points such as $B_z = \pm\infty$ as infinitely slow and continuous process is not required and achieve high-fidelity state transfer as shown in Fig. 4.

As a remark, we find that our jumping protocol with $N = 1$ (i.e., a Rabi pulse) specialises to the optimized composite pulse protocol [12] but has the advantage that no additional strong $\pi/2$ pulses at the beginning and the end of the evolution are required. Moreover, by applying the jumping protocol with $N = 1$ to the adiabatic passage proposed in Ref. [29], we obtain the protocol that has been used to experimentally generate Fock states of a trapped atom [30]. When, instead of a single target point, high-fidelity adiabatic evolution along the path is also desired, we can use the jumping protocol with a larger N. A large N not only increases the adiabatic fidelity along the path, but also grantees unit fidelity for N geodesic points.

In summary, we have demonstrated quantum adiabatic evolutions with energy crossings. We have shown that the quantum dynamic phases are more fundamental than energy gaps in quantum adiabatic processes. Thanks to rapid changes of these phases, non-adiabatic transitions can be suppressed and fast varying Hamiltonians can still realise quantum adiabatic evolutions. By going beyond the limit of non-zero energy gaps we demonstrate ex-
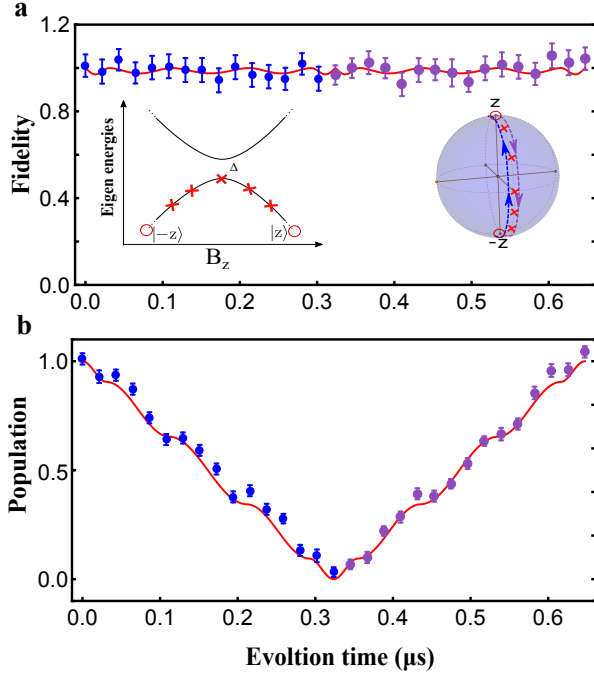
FIG. 4. **Avoiding unphysical points in the Landau-Zener model. a,** Measured state fidelity (dots) during the evolution time along the path of the Landau-Zener model by using the jumping protocol of $N = 5$ pulses. Left inset: the eigen energies of the Landau-Zener model have an avoid crossing $\Delta = 2\pi \times 5$ MHz. Right inset: the path was set as from the $-Z$ to Z (blue arrows) and back from Z to $-Z$ (purple arrows). The red crosses show the path points for the jumping protocol. The red circles indicate the $\pm Z$ path points that require an infinitely large B_z. **b,** Population at $|-z\rangle$ during the evolution time along the path. The red lines are the numerical simulations, and the target state is defined as the ideal adiabatic state driven under the control with an infinite number of π pulses.

perimentally fast quantum adiabatic protocols with unit fidelity in finite times, challenging the general belief that an infinite evolution time is a necessary condition for unit fidelity in quantum adiabatic evolution. Because our protocol uses the intrinsic adiabatic path that follows the eigenstates of the Hamiltonian, no intricate additional conterdiabatic control, which unavoidably changes the eigenstates of the initial Hamiltonian and introduces additional control errors, is required. As a consequence, our methods avoid the use of difficult or unavailable control resources and share the intrinsic robustness of adiabatic methods. By using the jumping along the path, unphysical points in the adiabatic path can be avoided.

METHODS

Adiabatic evolution along the geodesics

For two arbitrary states $|\Psi_i\rangle$ and $|\Psi_t\rangle$, one can write $\langle\Psi_i|\Psi_t\rangle = \cos\left(\frac{1}{2}\theta_g\right)e^{i\phi_{i,t}}$ with $\phi_{i,t}$ and θ_g being real. Here θ_g is the path length connecting $|\Psi_i\rangle$ and $|\Psi_t\rangle$ by the geodesic and we set $\phi_{i,t} = 0$ by a proper gauge transformation [23]. The geodesic [23, 24] that connects $|\Psi_i\rangle$ and $|\Psi_t\rangle$ by varying $\lambda = 0$ to $\lambda = 1$ can be written as $|\psi_1(\lambda)\rangle = c_i(\lambda)|\Psi_i\rangle + c_t(\lambda)|\Psi_t\rangle$, where the coefficients $c_i(\lambda) = \cos(\frac{1}{2}\theta_g\lambda) - \sin(\frac{1}{2}\theta_g\lambda)\cot(\frac{1}{2}\theta_g)$ and $c_t(\lambda) = \sin(\frac{1}{2}\theta_g\lambda)/\sin(\frac{1}{2}\theta_g)$ for $\sin(\frac{1}{2}\theta_g) \neq 0$. To describe $|\psi_1(\lambda)\rangle$ in terms of the system eigenstates, we choose an orthonormal state $|\psi_2(0)\rangle \propto (I - |\Psi_i\rangle\langle\Psi_i|)|\Psi_t\rangle$ if $\sin(\frac{1}{2}\theta_g) \neq 0$. When $|\Psi_t\rangle$ is equivalent to $|\Psi_i\rangle$ up to a phase factor (i.e., $\sin(\frac{1}{2}\theta_g) = 0$), $|\psi_2(0)\rangle$ can be an arbitrary orthonormal state. Then the geodesic can be written as $|\psi_1(\lambda)\rangle = \cos(\frac{1}{2}\theta_g\lambda)|\psi_1(0)\rangle + \sin(\frac{1}{2}\theta_g\lambda)|\psi_2(0)\rangle$ and its orthonormal state $|\psi_2(\lambda)\rangle = -\sin(\frac{1}{2}\theta_g\lambda)|\psi_1(0)\rangle + \cos(\frac{1}{2}\theta_g\lambda)|\psi_2(0)\rangle$. Along the geodesic we have $g_{2,1}(\lambda) = -g_{1,2}(\lambda) = i\frac{1}{2}\theta_g$ being a constant and $g_{n,m} = 0$ for other combinations of n and m. Along the geodesic if one changes the dynamic phases with a π phase shift only at each of the N equally spaced path points $\lambda_j = (2N)^{-1}(2j-1)$ with $j = 1, 2, \ldots, N$, the operators $W(\lambda)$ at different λ commute and $\int_0^1 F_{2,1}(\lambda)d\lambda = 0$. As a consequence, $U_{\mathrm{dia}}(1) = \exp\left[i\int_0^1 W(\lambda)d\lambda\right] = I$ and the quantum evolution $U = U_{\mathrm{adia}}$ does not have any non-adiabatic effects.

Adiabatic evolution by continuous driving with a constant gap

For the standard protocol that the driving amplitude is a constant, the driving Hamiltonian $H(\lambda) = \frac{1}{2}\Omega e^{-i\frac{1}{2}\sigma_z\theta_g\lambda}\sigma_\theta e^{i\frac{1}{2}\sigma_z\theta_g\lambda}$ is parameterized by $\lambda = t/T$ along a circle of latitude with $\sigma_\theta = \sigma_z\cos\theta + \sigma_x\sin\theta$ in a total evolution time T. The difference of the accumulated dynamic phases at $\lambda = 1$ on the two eigenstates is $\phi = \Omega T$. One can show that the system evolution at $\lambda = 1$ reads

$$U = e^{-i\frac{1}{2}\theta_g\sigma_z}\exp\left[-i\frac{1}{2}\left(\phi\sigma_\theta - \theta_g\sigma_z\right)\right]. \qquad (7)$$

The ideal adiabatic evolution is obtained by using equation (7) in the adiabatic limit $T \to \infty$ (i.e., $\phi \to \infty$),

$$U_{\mathrm{adia}} = \lim_{T\to\infty} U = e^{-i\frac{1}{2}\theta_g\sigma_z}e^{i\frac{1}{2}\theta_g\cos\theta\sigma_\theta}e^{-i\frac{1}{2}\phi\sigma_\theta}. \qquad (8)$$

Without the part of dynamic phases, U_{adia} describes geometric evolution and for a cyclic evolution $\theta_g = 2\pi$ the geometric evolution is described by the Berry's phases $\pm\pi(\cos\theta - 1)$. By comparing U_{adia} and U or by using the

results in Ref. 22, the non-adiabatic correction is given by

$$U_{\text{dia}} = \exp\left[i\frac{1}{2}\left(\phi - \theta_g \cos\theta\right)\sigma_\theta\right]U', \qquad (9)$$

with

$$U' = \exp\left[-i\frac{1}{2}\left(\phi\sigma_\theta - \theta_g\sigma_z\right)\right]. \qquad (10)$$

In the adiabatic limit $T \to \infty$ (i.e., $\phi \to \infty$), $U_{\text{dia}} = I$ is the identify operator. We note that when the phase factor of the state is irrelevant one can perform perfect state transfer by this driving if the initial state is prepared in an initial eigenstates of the driving Hamiltonian $H(\lambda)$ (i.e., the eigenstates of σ_θ). From equation (9), U_{dia} is diagonal in the basis of σ_θ when $U' \propto I$. As a consequence, with $|\Psi_i\rangle$ prepared as an eigenstate of σ_ϕ, the evolved state $U|\Psi_i\rangle$ matches the target state $U_{\text{adia}}|\Psi_i\rangle$ up to a phase factor when $U' \propto I$. For the case of the evolution along the geodesic $\theta = \pi/2$, when $\sqrt{\phi^2 + \theta_g^2} = 2k\pi$ ($k = 1, 2, \ldots$), which implies $U' \propto I$, the population transfer for the initial eigenstates of σ_x is perfect.

Numerical simulations

In the simulations, we used the Hamiltonian for the control on the $m_s = 0, 1$ levels,

$$H = (B_z + \delta_0)\frac{\sigma_z}{2} + [\Omega(t) + \delta_1](\cos\vartheta\frac{\sigma_x}{2} + \sin\vartheta\frac{\sigma_y}{2}), \quad (11)$$

where $\vartheta = \theta_g\lambda$, B_z is the detuning, and $\Omega(t)$ is the Rabi frequency for the control. δ_0 is the dephasing noise from static and time-dependent magnetic field fluctuations with a $T_2^* = 1.7$ μs. δ_1 is the random static changes in the driving amplitude. δ_0 follows the Gaussian distribution with the mean value $\mu = 0$ and the standard deviation $\sigma = 2\pi \times 130$ kHz. The probability density of δ_1 has the Lorentz form $f(\delta_1; \delta_{10}, \gamma) = 1/\{\pi\gamma[1+(\frac{\delta_1-\delta_{10}}{\gamma})^2]\}$ with $\delta_{10} = 1$ and $\gamma = 0.0067$. All the parameters in the distribution function are extracted from fitting the free induction decay (FID) and the decay of Rabi oscillation.

Experimental Setup

The experiments were performed with a home-built optically detected magnetic resonance (ODMR) platform, which consists of a confocal microscope and a microwave (MW) synthesizer (Supplementary Fig. 5). A solid state green laser with 532 nm wavelength is used for initializing and reading out the NV spin state. The light beam was focus on the NV center through an oil immersion objective (N.A., 1.4). The emitted fluorescence from NV center was collected by a single photo counting module (APD). Here we used an NV center embedded in a room-temperature bulk diamond grown by chemical vapour

deposition with [100] faces. It has ^{13}C isotope of natural abundance and nitrogen impurity less than 5 ppb. To lift the degeneracy of the $|m_s = \pm 1\rangle$ states, a static magnetic field of 510 G was provided by a permanent magnet. The magnetic field was aligned by adjusting the three-dimensional positioning stage on which the magnet was mounted, and simultaneously monitoring the counts of the NV center. The direction of the magnetic field is well aligned when the counts shows no difference between with and without the magnet. Manipulation of the NV center is performed by MW pulse applied through a home-made coplanar waveguide (CPW). The MW pulse was generated by the I/Q modulation of the Agilent arbitrary wave generator (AWG) 81180A and the vector signal generator (VSG) E8267D then amplified by Mini Circuits ZHL-30W-252+. An atomic clock was used to synchronize the timing of the two. The AWG supplies the I and Q data with frequency of 400 MHz, and the VSG generates the 3898 MHz carrier. The output frequency is 4298 MHz, which matches the transition frequency between the NV $m_s = 0$ and $m_s = +1$ states.

Experimental Sequences

As the magnetic field is 510 G, we first applied the green laser for 3 μs to initialize the NV center electronic spin to the level of $m_s = 0$ and the adjacent ^{14}N nuclear spin simultaneously [31]. The preparation of the NV electron spin in an equal superposition state of $m_s = 0$ and $m_s = 1$ was realized by applying a MW $\pi_x/2$ ($\pi_y/2$) pulse, i.e., by the rotation around the x (y) axis with an angle of $\pi/2$. Then the NV electron spin was driven according to a desired path. To experimentally characterize the evolution path, we sampled the path with several points and measured the spin state through tomography. $\pi_x/2$ or $\pi_y/2$ pulses were applied to readout the off-diagonal terms. Finally the spin state was read out by applying the laser pulse again and measuring the spin-dependant fluorescence. Typically the whole sequence was repeated 10^5 times to get better signal to noise ratio (SNR). The schematic diagram of the pulse sequence is shown in Supplementary Fig. 6.

In driving the NV electron spin along the path given by equation (5), we used an on-resonant MW field and swept the MW phase $\theta_g\lambda$ with the path parameter λ. In driving the NV electron spin along the path of the LZ Hamiltonian, the MW phase was a constant, Δ was set by the Rabi frequency, and B_z was the MW frequency detuning which varied as $B_z = -\Delta\cot(\theta_g\lambda)$. For continuous driving, the path parameter λ varies with a constant rate $d\lambda/dt = f_{\text{rot}}$. In the jumping protocol λ jumps from point to point: $\lambda = \lambda_j = (2N)^{-1}(2j - 1)$ for $j = 1, 2, \ldots, N$. In this work the jumping protocol has a constant driving Rabi frequency Ω_0 and $\lambda = \lambda_j$ if $(j - 1)T/N \leq t < jT/N$ for a path with N pulses applied in a total time T. In the experiments with the back-forward motion along the geodesic, we reversed the

order of the parameter λ in the backward path. That is, in the jumping protocol we repeat the subsequent parameters $(\lambda_1, \lambda_2, \ldots, \lambda_{N-1}, \lambda_N, \lambda_N, \lambda_{N-1}, \ldots, \lambda_2, \lambda_1)$, while for the standard protocol of continuous driving we used the rate $d\lambda/dt = f_{\rm rot}$ for a forward path and the rate $d\lambda/dt = -f_{\rm rot}$ for a backward path and repeated the process.

We removed the irrelevant dynamic phases if the initial state was not prepared in an initial eigenstate to reveal the geometric evolution. At the beginning of state readout, we compensated the dynamic phases by applying an additional driving with a microwave π phase shift (i.e., $\Omega \to -\Omega$) at the point of the target state for a time equalling to the time for adiabatic evolution. This additional driving did not change the geometric phases and state transfer because it was applied at the final path point.

ACKNOWLEDGEMENTS

AUTHOR CONTRIBUTIONS

J.D. supervised the entire experiment. Z.Y.W. and M.B.P. formulated the theory. J.D. and F.S. designed the experiments. K.X., X.X., and P.W. prepared the setup. K.X. and T.X. performed the experiment. T.X., Z.Y.W. and K.X. performed the simulation. Z.Y.W., K.X., T.X., M.B.P., Y.W., and J.D. wrote the manuscript. All authors discussed the results and commented on the manuscript.

[1] Vitanov, N. V., Rangelov, A. A., Shore, B. W. & Bergmann, K. Stimulated Raman adiabatic passage in physics, chemistry, and beyond. *Rev. Mod. Phys.* **89,** 015006 (2017).

[2] Vitanov, N. V., Halfmann, T., Shore, B. W. & Bergmann, K. Laser-induced population transfer by adiabatic passage techniques. *Annu. Rev. Phys. Chem.* **52,** 763-809 (2001).

[3] Farhi, E., Goldstone, J., Gutmann, S. & Sipser, M. Quantum Computation by Adiabatic Evolution. Preprint at https://arxiv.org/abs/quant-ph/0001106 (2000).

[4] Jones, J. A., Vedral, V., Ekert, A. & Castagnoli, G. Geometric quantum computation using nuclear magnetic resonance. *Nature* **403,** 869-871 (1999).

[5] Barends, R. *et al.* Digitized adiabatic quantum computing with a superconducting circuit. *Nature* **534,** 222-226 (2016).

[6] Kim, K. *et al.* Quantum simulation of frustrated Ising spins with trapped ions. *Nature* **465,** 590-593 (2010).

[7] Biamonte J., Bergholm V., Fitzsimons J. & Aspuru-Guzik A. Adiabatic quantum simulators. *AIP Adv.* **1,** 022126 (2011).

[8] Born, M. & Fock, V. Beweis des Adiabatensatzes. *Z. Phys.* **51,** 165 (1928).

[9] Demirplak, M. & Rice, S. A. Adiabatic Population Transfer with Control Fields. *J. Phys. Chem. A* **107,** 9937-9945 (2003).

[10] Berry, M. V. Transitionless quantum driving. *J. Phys. A* **42,** 365303 (2009).

[11] Chen, X., Lizuain, I., Ruschhaupt, A., Guéry-Odelin, D. & Muga, J. G. Shortcut to adiabatic passage in two- and three-level atoms. *Phys. Rev. Lett.* **105,** 123003 (2010).

[12] Bason, M. G. *et al.* High-fidelity quantum driving. *Nat. Phys.* **8,** 147-152 (2012).

[13] Torrontegui, E. *et al.* Shortcuts to Adiabaticity, *Adv. At. Mol. Opt. Phy.* **62,** 117 (2013).

[14] Deffner, S., Jarzynski, C. & del Campo, A. Classical and Quantum Shortcuts to Adiabaticity for Scale-Invariant Driving. *Phys. Rev. X* **4,** 021013 (2014).

[15] Zhou, B. B. *et al.* Accelerated quantum control using superadiabatic dynamics in a solid-state lambda system. *Nature Phys.* **13,** 330-334 (2017).

[16] Doherty, M. W. *et al.* The nitrogen-vacancy colour centre in diamond. *Phys. Rep.* **528,** 1-45 (2013).

[17] Childs, A. M., Farhi, E. & Preskill, J.. Robustness of adiabatic quantum computation. *Phys. Rev. A* **65,** 012322 (2001).

[18] Berry, M. V. Quantal phase factors accompanying adiabatic changes. *Proc. R. Soc. Lond. A* **392,** 45-57 (1984).

[19] Wilczek, F. & Zee, A. Appearance of gauge structure in simple dynamical systems. *Phys. Rev. Lett.* **52,** 2111-2114 (1984).

[20] Marzlin, K.-P. & Sanders, B. C. Inconsistency in the Application of the Adiabatic Theorem. *Phys. Rev. Lett.* **93,** 160408 (2004).

[21] Tong, D. M., Singh, K., Kwek, L. C. & Oh, C. H. Quantitative Conditions Do Not Guarantee the Validity of the Adiabatic Approximation. *Phys. Rev. Lett.* **95,** 110407 (2005).

[22] Wang, Z.-Y. & Plenio, M. B. Necessary and sufficient condition for quantum adiabatic evolution by unitary control fields. *Phys. Rev. A* **93,** 052107 (2005).

[23] Anandan, J. & Aharonov, Y. Geometry of quantum evolution. *Phys. Rev. Lett.* **65,** 1697 (1990).

[24] Chruscinski, D. & Jamiolkowski, A. Geometric Phases in Classical and Quantum Mechanics (Birkhäuser, 2004).

[25] Yang, W., Wang, Z.-Y. & Liu, R.-B. Preserving qubit coherence by dynamical decoupling. *Front. Phys.* **6,** 2-14

(2011).

[26] Shevchenko, S., Ashhab, S. & Nori, F. Landau-Zener-Stuckelberg interferometry. *Phys. Rep.* **492,** 1-30 (2010).

[27] Sun, G. *et al.* Observation of coherent oscillation in single-passage Landau-Zener transitions. *Sci. Rep.* **5,** 8463 (2015).

[28] Foletti, S., Bluhm, H., Mahalu, D., Umansky, V. & Yacoby, A. Universal quantum control in two-electron spin quantum bits using dynamic nuclear polarization. *Nature Phys.* **5,** 903-908 (2009).

[29] Cirac, J. I., Blatt, R. & Zoller, P. Nonclassical states of motion in a three-dimensional ion trap by adiabatic passage. *Phys. Rev. A* **49,** R3174(R) (1994).

[30] Meekhof, D. M., Monroe, C., King, B. E., Itano, W. M. & Wineland, D. J. Generation of nonclassical motional states of a trapped atom. *Phys. Rev. Lett.* **76,** 1796-1799 (1996).

[31] Epstein, R. J., Mendoza, F. M., Kato, Y. K. & Awschalom, D. D. Anisotropic interactions of a single spin and dark-spin spectroscopy in diamond. *Nature Phys.* **1,** 94-98 (2005).
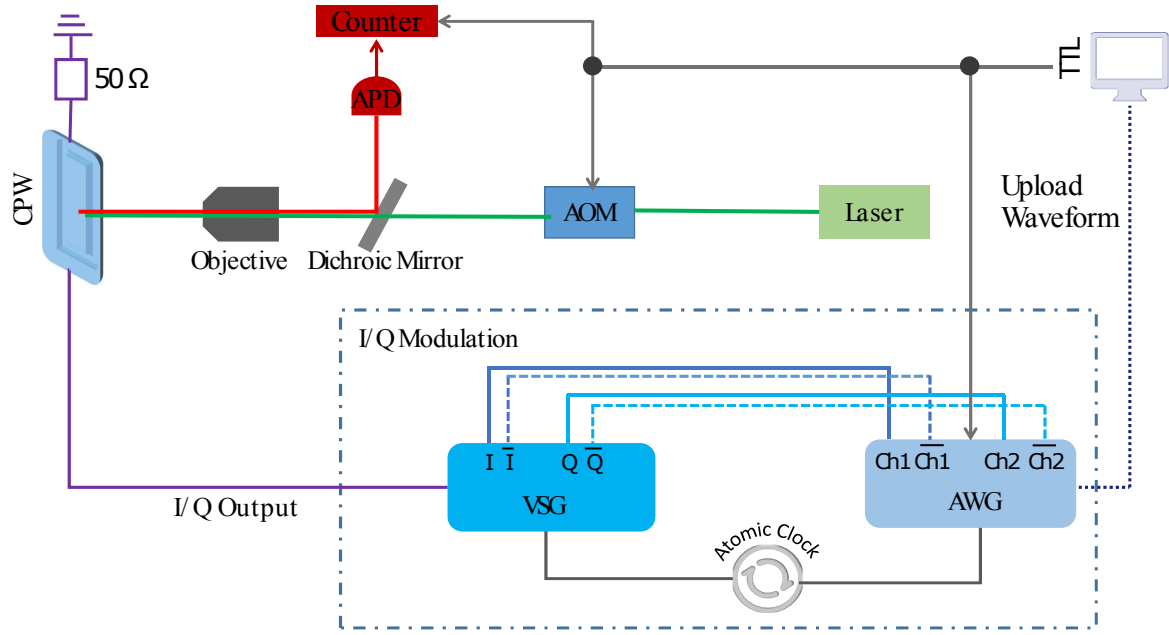
FIG. 5. **Sketch of the experimental setup.** The whole setup mainly consists of two parts: a home-built confocal microscopy and a microwave synthesizer. The microwave used to control the spin evolution was generated through I/Q modulation. The desired waveform was uploaded form the PC to the AWG. The two separated channels on the AWG generated the I and Q signal respectively and transmitted to the VSG, then the VSG did the I/Q modulation. An atomic clock was used to synchronize the AWG and VSG. A pulse blaster served to provide TTL signals to control the switch of the AWG and AOM, and also the time bin of the counter.
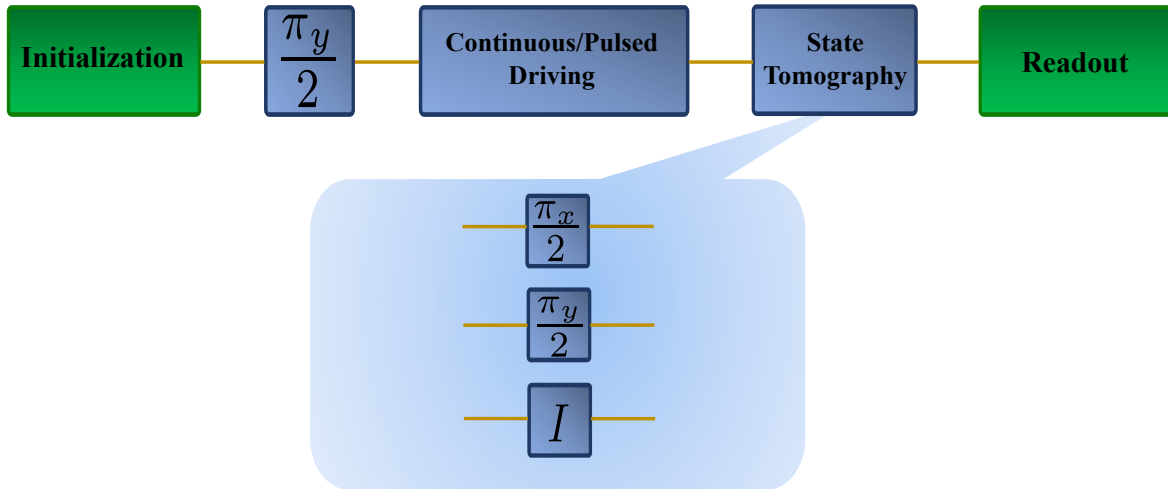
FIG. 6. **Experimental pulse sequence.** Green laser was applied in the beginning to initialize the electronic spin and at the end to readout the spin state. The first $\pi_y/2$ pulse set the spin state to be aligned with $+x$ axis, then the continuous or pulsed driving scheme let the spin state go back-forward along the equator. When doing the quantum state tomography, three different kinds of pulses were applied, i.e., $\pi_x/2$, $\pi_y/2$ and identity operator.
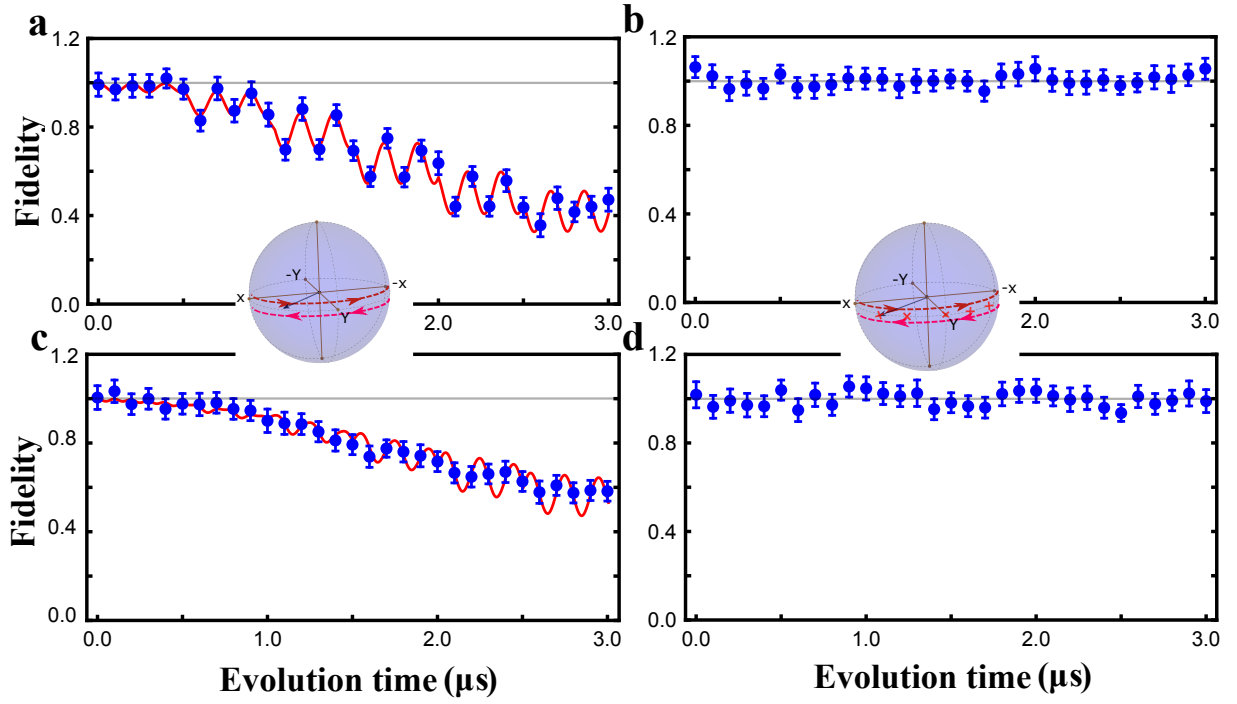
FIG. 7. **Comparison of the fidelity of adiabatic process between continuous and jumping protocols during the evolution.** Both protocols use the same amplitude of Rabi frequency $\Omega_0 = 2\pi \times 5$ MHz as in Fig. 2 of the main text. The blue dots are the fidelities of the experimental state to the target state, the red lines are the fidelities of the theoretically calculated state to the target state. In both cases, the target states are defined as the ideal state under infinitely slow adiabatic evolution. The grey horizontal line indicates where the unity fidelity lies. In **a** and **b** the initial state is prepared in $|+_0\rangle$, while **c** and **d** are the results when the initial state starts from $|+_{1/2}\rangle$, which is an equal superposition of the states $|\pm_0\rangle$.
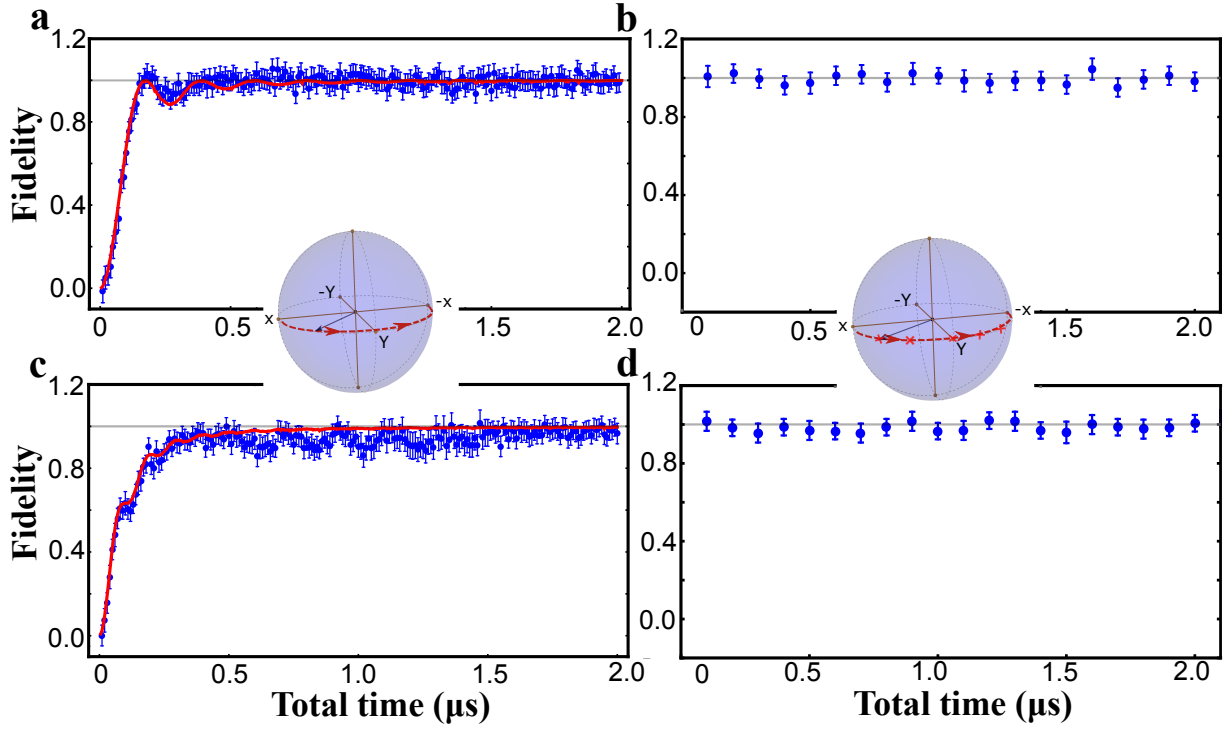
FIG. 8. **Comparison of the fidelity of state transfer as a function of total time between standard (continuous) and jumping (pulsed) schemes with only forward evolution.** The crosses on the Bloch sphere in the inset on top of **b** and **d** indicate the path points for the case of $N = 5$. In **a** and **b** (**c** and **d**) the initial state is prepared in $|+_0\rangle = |x\rangle$ ($|+_{1/2}\rangle = |y\rangle$). The fidelities of the red lines and the blue dots adopt the same definitions in Fig. 2 of the main text.
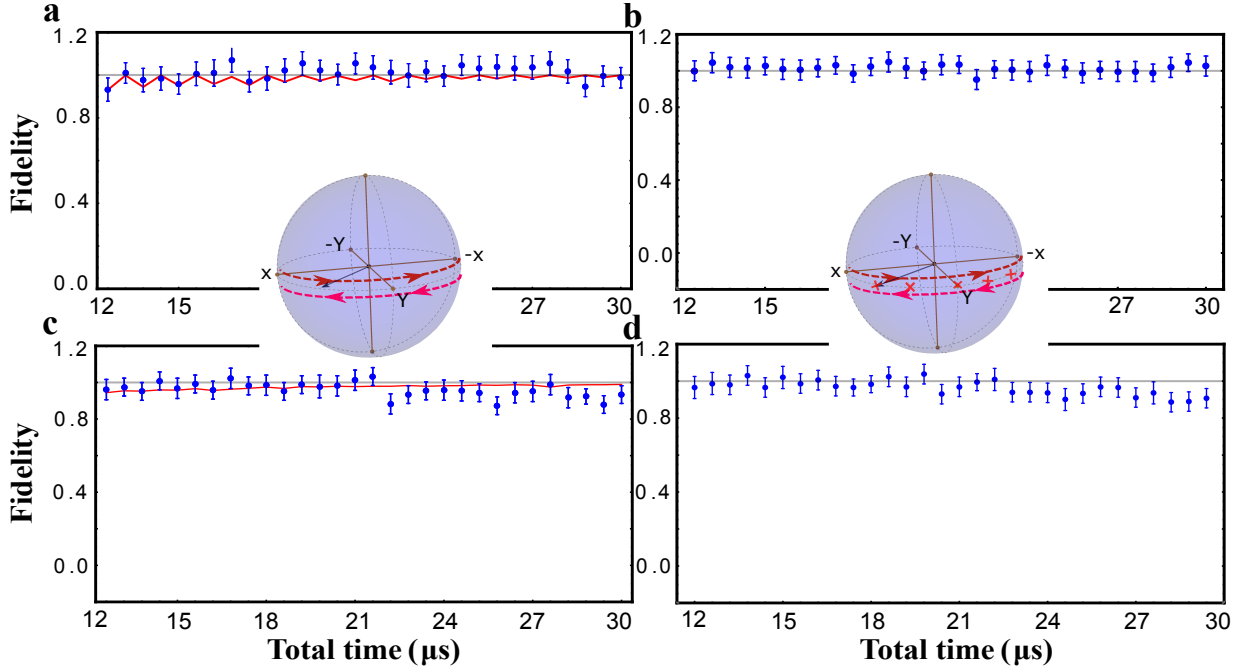
FIG. 9. **Adiabatic evolution for a rather long time compared with the NV coherence time. a,c** and **b,d** show the final state fidelity to the target adiabatic state with total time by using the continuous protocol and the jumping protocol, respectively. The insets illustrate the path that goes from the X direction to the $-$X direction via a geodesic half circle then travels back to X and repeats the back-forward motion for three times. In **a** and **b** (**c** and **d**) the initial state is prepared in $|+_0\rangle = |x\rangle$ ($|+_{1/2}\rangle = |y\rangle$). The target state here is defined the same as the one in Fig. 2 of the main text.
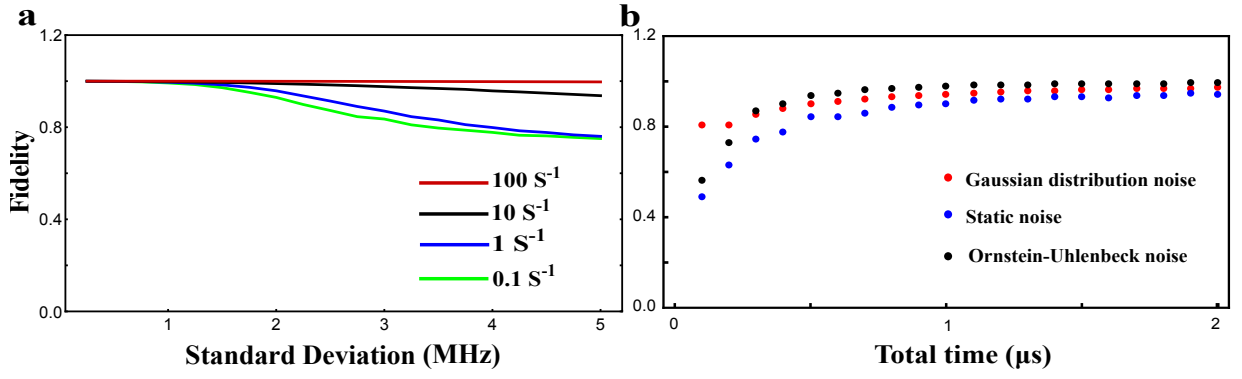
FIG. 11. **a: Ornstein-Uhlenbeck process modelled noise with varying decay rates.** The simulations show that the fidelity decays slower as the decay rate β goes higher. The red, blue, black and green lines correspond to $\beta = 100$, 10, 1 and 0.1 s^{-1}, respectively.**b: Noise acting on the adiabatic process with varying total times.** The red, blue and black dots correspond to the un-correlated Gaussian distribution noise, static noise, and Ornstein-Uhlenbeck process modelled noise, respectively. The parameters in these noise models are the same as the ones chosen in Fig. 10.